This article has been accepted for publication in a future issue of this journal, but has not been fully edited. Content may change prior to final publication. Citation information: DOI 10.1109/TIM.2019.2956421, IEEE Transactions on Instrumentation and Measurement

On the feasibility of Absolute Distance Measurement by using Optical-Feedback into a Superluminescent Diode Cavity

Luigi Rovati, *Member, IEEE*, Luca Di Cecilia, and Stefano Cattini, *Member, IEEE,*

***Abstract*—The development of accurate absolute distance interferometers is a long-term research goal. The key impact of this paper is the demonstration of an absolute distance interferometer based on the optical-feedback into a superluminescent diode cavity. Thanks to the optical-feedback, we obtained huge interference fringes even with diffusive targets and without using high-sensitivity and low-noise detectors, but directly exploiting the monitor photodiode enclosed in the same package of the optical source.**

The low coherence of the optical source makes the system robust to any stray-light along the optical path and thus suitable to work in biological media and dusty industrial environments. The proposed signal processing exploits a zero-crossing approach to determine the absolute target position. Preliminary results show a 95% expanded uncertainty to measuring interval ratio of about 60 ppm over a measuring interval of 50 mm.

***Index Terms*—Measurement techniques, Optical interferometry, Length measurement, Low-coherence interferometry, Self-mixing, Optical-feedback, Absolute distance measurement, Superluminescent diode.**

I. Introduction

Low-coherence interferometry (LCI) is a well-established interferometric technique that is nowadays used in multiple applications, both industrial and medical [1]–[3]. The presence of multiple wavelengths is the basis of LCI. Since interference substantially occurs only between fields having optical path difference (OPD) shorter than the coherence length of the source, LCI generally allows to better define the region under test even in diffusive media or in the presence of significant straylight. This fact has been widely exploited to carry out measurements of absolute distance [4] or precise flow analysis [5]. A typical example of the interferometric use of low-coherence sources is the Optical Coherence Tomography i.e. OCT [6], [7]. Such technique is based on the light generated by a superluminescent diode (SLD) that is guided by a single mode fiber on living tissues (typically ocular tissues); light back-scattered from the different layers is collected and the signal resulting from the interference with a reference beam is detected using high-sensitivity and low-noise detectors, allowing reconstructing in-vivo three-dimensional map of tissues.

The optical setup of interferometric systems can be greatly simplified without sacrificing performance by introducing an optical-feedback (OF) also known as self-mixing (SM). OF in semiconductor optical sources, traditionally laser diodes (LDs), is of increasing importance for metrological purposes [8]. Interferometry, vibrometry, Doppler velocimetry and, in general, dimensional measurements represent the major metrological fields of application [9]–[17]. LCI and OF can be advantageously integrated to obtain compact interferometric systems. Indeed, like laser diodes, also SLDs generally have a monitor photodiode PD enclosed in the package of the optical source on the emitting junction backface. As in self-mixing laser diode (SM-LD) interferometry, this photodiode can be used to detect the interferometric signal also taking advantage of the high-gain active region of the source.

In this paper, we extend the theory, analysis and results we previously presented at I2MTC 2019 [18] on how OF into an SLD cavity can be exploited to perform absolute distance measurements.

In particular, section II briefly introduces the self-mixing interferometry and reviews the relative state of the art. Section III describes the proposed measuring system, the measurement model and the performed experimental activities. The obtained results are reported in section IV and conclusions are drawn in section V. Finally, appendix A investigates the ultimate system performances.

II. Theoretical Background

Optical-feedback is generated by back-diffusion and/or reflection of part of the emitted beam back into the active region of the source. This phenomenon is more advantageously exploitable for interferometric measurements if the source includes in the same package a monitor photodiode, i.e. LDs and SLDs. In this case, the optical setup is very simple because the same component acts as both source and detector.

As shown in Fig. 1, for coherent sources the reference beam P_0^* is the one emitted by the emitting junction backface, whereas the measurement beam P_0/A originates from the reflection on the target of the emitted beam P_0, such reflection is then re-injected in the optical cavity of the source, where the returning field modulates (in AM and FM) the in-cavity field and the result is detected by the monitor photodiode. Therefore, the SM interferometric setup includes the cavity of the coherent source and an external cavity.

Since with low-coherence sources (SLDs) the returning field is generally delayed beyond the coherence length l_c of the source and thus cannot interfere with the cavity field, for self-mixing low-coherence interferometry two external fields of

L. Rovati and S. Cattini are with the Department of Engineering "Enzo Ferrari", University of Modena and Reggio Emilia, Via Vivarelli 10, 41125, Modena, Italy. e-mail: luigi.rovanti@unimore.it

L. Di Cecilia is with CNH Industrial Italia Spa, Viale delle Nazioni, 55, 41122 Modena, Italy

Manuscript received XXX, XXX; revised XXXX.

This article has been accepted for publication in a future issue of this journal, but has not been fully edited. Content may change prior to final publication. Citation information: DOI 10.1109/TIM.2019.2956421, IEEE Transactions on Instrumentation and Measurement

comparable optical pathlength are required as shown in Fig. 2. The SLD cavity works in this case as an optical amplifier [19] and the so obtained interferometric signal is then optically amplified by the high-gain active region of the source making its detection simpler and thus enhancing the signal-to-noise ratio. Indeed, given: i) the amplification of the returning signal performed by the optical gain in the source (up to 30 dB in high power SLDs [20]), ii) the little residual mirror reflectivity and iii) the efficient power collection of the returning field, to avoid emission instabilities or damages to the source, an optical attenuator is sometimes used to adjust the level of returning optical signal.

A. Self-mixing Interferometry Based on Coherent Sources

Self-mixing interferometry based on coherent sources is a well-established technique for distance and displacement measurements [21]–[28].

As previously introduced, in contrast to "classic" interferometers that split the beam and recombine it on a detector external to the source thus avoiding the laser beam to re-enter the laser cavity, in self-mixing a fraction of the power emitted by the source is collected back into the cavity and usually detected by the back-facet monitor photodiode PD generally embodied to monitor the power emitted by the source. This arrangement not only minimizes the number of components but also optically amplifies the interferometric signal thanks to the high-gain active medium, thus simplifying preamplification and resulting in less sensitive to environmental noise and electromagnetic interference [29].

Indeed, according to Donati [30], self-mixing interferometers based on coherent sources inherently have the following advantageous features:

- optical part-count is minimal,
- setup is self-aligned,
- no spatial, wavelength or stray-light filters required,
- operates on a normal diffusing target surface,
- resolution is $\lambda/2$ with fringe counting and sub-λ with analog processing,
- bandwidth is up to hundreds of kHz or MHz,
- signal is everywhere on the beam, also at the target side.

The possibility to exploit P_0^* as reference beam simplify the optical layout, nevertheless SM approach based on a coherent source suffers the same limitations as "classic" coherent interferometers since stray-light due to potential unwanted reflection or diffusion of the measurement beam P_0 gives rise to the well-known cyclic error [31].

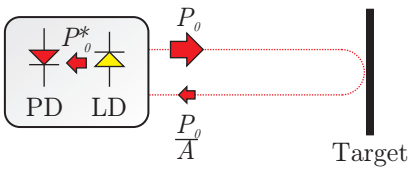

Fig. 1. The basic setup of an interferometer based on OF in a laser diode (LD). The beam from the LD illuminates a remote target and a fraction $1/A$ of the emitted power P_0 is collected back into the cavity, where it leads to modulation of the cavity electromagnetic field. The monitor photodiode PD detects the resulting interferometric signal.

B. Self-mixing Interferometry Based on Low-Coherence Sources

LCI is inherently robust to potential stray-light due to unwanted reflection or diffusion of the measurement beam since the coherence length l_c of the optical source is inversely proportional to its spectral bandwidth

$$l_c = \frac{c}{n \cdot \Delta\nu_{eff}} \ , \tag{1}$$

where c is the speed of light, n is the refractive index and, $\Delta\nu_{eff}$ is the effective optical line width of the source. For Gaussian sources

$$\Delta\nu_{eff} = \frac{\Delta\nu}{\sqrt{2\ln 2/\pi}} \ , \tag{2}$$

and the coherence length can be written equivalently as:

$$l_c = \frac{\bar{\lambda}^2 \cdot \sqrt{2\ln 2/\pi}}{n \cdot \Delta\lambda} \ , \tag{3}$$

where $\Delta\nu$ and $\Delta\lambda$ are the full width at half maximum of the power spectrum of the source in the frequency and wavelength domains and $\bar{\lambda}$ is the emission peak wavelength. Fields having an optical path difference (OPD) greater than l_c give rise to statistically null interference. Hence, light back-diffused and/or reflected by the target cannot interfere with the electromagnetic field in the source cavity (P_0^*). Therefore, to generate an interferometric signal, at least two external cavities, one of which defined by the target, are required. Indeed, only fields having a path difference shorter than the source coherence length l_c substantially contribute to the interferometric signal [32].

With reference to a SLD, possible setups of a self-mixing interferometer based on a low-coherence source are shown in Fig. 2. Note that only configurations in Fig. 2(a) and Fig. 2(b) are suitable for absolute distance measurements. In particular, Fig. 2(a) shows a "Michelson-like" architecture where the interference is obtained exploiting the field reflected by the mirror Mr (P_0/A_1) as the reference beam. The architecture shown in Fig. 2(b) is a "Fizeau-like" interferometer where the reference beam is obtained exploiting a double reflection by the semireflecting slab (SS). Part of P_0 (P_0/A_3) is back-reflected by SS, but it cannot interfere with the beam from the Target (P_0/A_2) since their OPD is much higher than the coherence length of the SLD. The reference beam is thus obtained exploiting the second reflection of P_0/A_3 beam which retraces the main beam back to SS giving rise to P_0/A_1. Interference is thus obtained once SS is at a distance from the SLD equal to half the distance between the SLD and the Target. Given such double reflection by SS the power falls quickly, thus the architecture shown in Fig. 2(b) can generally only be used with nearby targets (few centimeters). Finally, setup in Fig. 2(c) can be used for flow measurements exploiting the reflection from the internal wall of the duct (P_0/A_1) as the reference arm [33].

C. SLD: Optical spectrum, effects of the optical-feedback and operating modes

SLDs are semiconductor devices capable to produce output power densities similar to ones produced by LDs with an

This article has been accepted for publication in a future issue of this journal, but has not been fully edited. Content may change prior to final publication. Citation information: DOI 10.1109/TIM.2019.2956421, IEEE Transactions on Instrumentation and Measurement

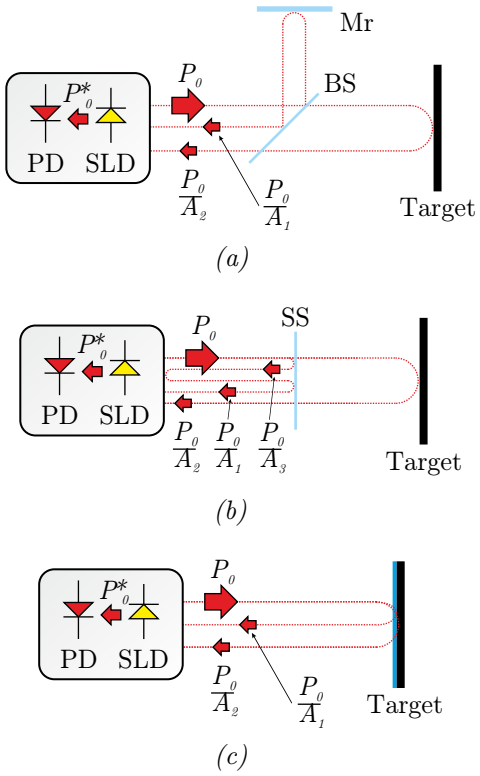

Fig. 2. Basic setups of an interferometer based on OF in a superluminescent diode (SLD). The beam generated by the SLD is shone onto the target and at least two fractions $1/A_1$ and $1/A_2$ of the emitted power P_0 are collected back into the cavity, where they are amplified. The beating of such beams is finally detected by monitor photodiode PD. P_0^* is the optical power emitted by the rear face of the light source. Figure (a) shows a "Michelson-like" layout: the beam splitter (BS) and the mirror (Mr) are used to realize the two external cavities. Figure (b) shows how a semireflecting slab (SS) can be used to obtain two co-axial external cavities as proposed by Rovati et al. [34]. In figure (c) interference is obtained without additional components by exploiting multiple feedbacks with different optical paths generated by the Target, as we proposed in our previous paper [33].

optical spectrum as broad as a LED. As a result, SLDs usually result the source of choice for LCI.

The high power densities and broad optical spectrum in SLD are obtained thanks to an high optical gain and gain spectrum in SLD active region and generally with minimal reflections from both ends of the active cavity [35]. However, the SLD spectrum usually presents a parasitic Fabry-Perot modulation due to residual reflections from SLD facets. The resulting spatial period of this modulation is [35]:

$$\lambda_{FSR} = \frac{\bar{\lambda}^2}{2n^* L_a} \ , \tag{4}$$

where L_a is the cavity length, and n^* is the effective refractive index for the optical mode ($n^* L_a$ is the effective cavity length). Such residual Fabry-Perot modulation gives also rise to the so-called "secondary coherence effects", which produces subpeaks in coherence function at $OPDs$ multiple integers of $2n^* L_a$. The amplitude of such secondary subpeaks is determined by the "integral" value of Fabry-Perot modulation across the entire spectrum [35].

The very high optical gain in the active region results in a very high sensitivity of SLDs to OF [20]. According to Shidlovski [20], OF in SLDs modify the spectrum both in terms of shape and ripple. In particular, under OF the spectrum generally suffers higher degradation at "short wavelength" [20].

III. Materials and Methods

A. Measuring System

The proposed measuring system is based on a low-cost pigtail SLD (model SLD-381-MP-DBUT-SM-PD, Superlum). Since the optical gain in semiconductors strongly depends on temperature, the SLD was mounted inside a temperature-controlled mount (TCM, model MDBUT, Superlum) driven by a thermoelectric temperature controller (TEC, model TED200C, Thorlabs) and the working temperature was fixed at 25°C.

As shown in Fig. 3, given the limited measuring interval of the architecture shown in Fig. 2(b), we realized an optical setup based on the configuration in Fig. 2(a).

The light generated by the pigtail SLD is guided by a single mode optical fiber to a non-contact receptacle-style collimator (CO, model HPUCO-23-850-S-2.7AS, OZ Optics) to feed the interferometer. The beam splitter BS — obtained by exploiting a thin, optical grade polycarbonate slab (refractive index $n \approx 1.57$ at $\bar{\lambda}$, reflectance about 5%) — divides the collimated beam into the two arms of the interferometer.

The reference arm consists in the movable mirror Mr that can be translated manually or by a direct current motor.

As a diffusing target, we use a simple loudspeaker driven by the function generator Fg. The neutral density filter NDF (OD = 1.6, transmission = 2.5%) attenuates the OF into the cavity to avoid damages and instabilities in the SLD.

A picture of the developed measuring system is shown in Fig. 4.

The current signal generated by the monitor photodiode PD is preamplified and converted into a voltage by the AC coupled transimpedance preamplifier Pa. The preamplifier feedback was designed to obtain a bandwidth of about 7 kHz and an in-band transimpedence of 50 kΩ.

As described in more detail in subsection III-B, the Target position x_{Target} is estimated from the maximum of the interferometric signal at the output of Pa. Therefore, the Pa output signal V1 is processed by an envelope detector (ED), a derivative circuit (TD), and a zero-crossing discriminator (ZCD).

Since in our measuring system the target distance x_{Target} is estimated as the Mr distance x_{Mr} that gives rise to $OPD = 0$ (see subsection III-B), the measuring interval of the system is mainly determined by the positioning and travel range of Mr. In our experimental setup such travel range was about 50 mm in addition to the zero-point fixed at about 3 cm from the point where BS divides the two beams.

As shown in Fig. 3, the setup of the measuring system also includes the "optional block" composed by the fused couplers/splitters (FCS, model 22-830-5/125-95/5, OZ Optics — 95/5 splitting ratio) and an optical spectrum analyzer (OSA, model MS9710C, Anritsu). Such optional block has been used for the analysis of the emission spectrum under optical-feedback as it will be described in subsection III-C.

This article has been accepted for publication in a future issue of this journal, but has not been fully edited. Content may change prior to final publication. Citation information: DOI 10.1109/TIM.2019.2956421, IEEE Transactions on Instrumentation and Measurement

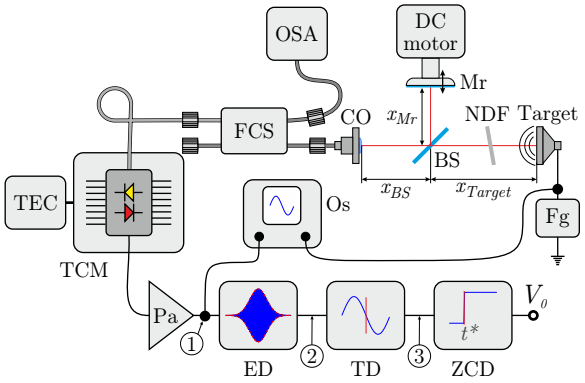

Fig. 3. Setup of the measuring system. The source is a low-cost pigtail SLD driven by custom electronics. The beam generated by the SLD is focused by the collimator CO and the beam splitter BS divides the collimated beam into the two arms of the interferometer. The reference arm consists in the movable mirror Mr that can be translated manually or by a direct current motor. The neutral density filter NDF attenuates the OF into the cavity to avoid damages and instabilities. As a diffusing target, we used a simple loudspeaker driven by the function generator Fg. The current signal generated by the monitor photodiode PD is preamplified and converted into a voltage by the AC coupled transimpedance preamplifier Pa. The Pa output is processed by the envelope detector ED, the time-derivative circuit TD, and the zero-crossing discriminator ZCD. Oscilloscope Os is used to observe the loudspeaker driving signal and the corresponding interferometric signal at the output of Pa. The "optional block" consisting of the 95/5 fused couplers/splitters FCS and the optical spectrum analyzer OSA allows real-time monitoring of the SLD spectrum.

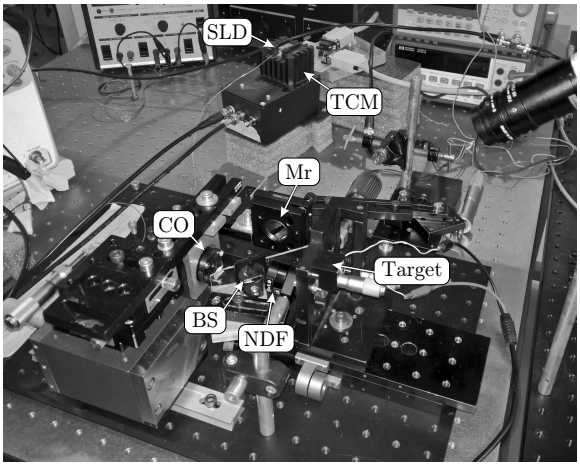

Fig. 4. Picture of the developed measuring system. In the figure it is possible to see the collimator CO, the beam-splitter BS, the neutral density filter NDF, the Target, the mirror Mr, the SLD and the temperature-controlled mount TCM.

B. Measurement Model and Procedure

According to Fig. 2(a), assuming linearly polarized "monochromatic" waves and supposing the SLD emission spectrum to be not perturbed by the fields re-entering the active medium — weak feedback—, the alternating component of the detected optical intensity I becomes:

$$I_{AC} \propto \gamma \cdot G_s \cdot 2 \sum_{i=1}^{N} (\mathbf{E}_{Si} \cdot \mathbf{E}_R) \cdot \Re\Big[\gamma_{S_iR}(OPD_{S_iR})\Big] \,, \quad (5)$$

where G_s is the single-pass net optical power gain coefficient, $\mathbf{E}_R$ is the amplitude of the electric field relative to the "reference beam" ("reference arm" — P_0/A_1), N is the number of fields reflected or back-diffused by the measurand that are simultaneously collected (P_0/A_2), $\mathbf{E}_{Si}$ is the amplitude of the i^{th} electric field reflected or back-diffused by the measurand, $\Re\{\}$ is the real part and, $\gamma_{S_iR}(OPD_{S_iR})$ is the complex degree of coherence between the $\mathbf{E}_R$ and $\mathbf{E}_{Si}$ fields (OPD_{S_iR} is the optical path pathlength difference between the two). In (5) N fields have been considered to take into account both targets having rough surfaces made by several elements, each of which contributing to the total returned field — speckle pattern regime — and, diffusing target such as biological tissues. On the other hand, in (5) the homodyne terms have been neglected since $N > 1$ is in general associated with diffusive measurand for which $|\mathbf{E}_{Si}| \ll |\mathbf{E}_R|$ can be commonly assumed. The complex degree of coherence can be written as [36]

$$\gamma_{S_iR} = |\gamma_{S_iR}| \exp\left[j\Big(\alpha_{S_iR} - 2\pi OPD_{S_iR}/\bar{\lambda}\Big)\right] , \quad (6)$$

where

$$\alpha_{S_iR}(OPD_{S_iR}) = \arg\left(\gamma_{S_iR}\right) + 2\pi OPD_{S_iR}/\bar{\lambda} \,. \quad (7)$$

According to the Wiener-Khintcine theorem, the complex degree of coherence is obtained by the Fourier transform of the power spectral density of the light source [37] (such is the basis of the Fourier spectroscopy). Hence, according to (5) the shape, spectral bandwidth ($\Delta\lambda$), center wavelength ($\bar{\lambda}$) and residual spectral modulation (i.e. parasitic Fabry-Perot modulation) of the light source have a deep impact on the γ_{S_iR}.

As it will be shown in Figs. 8 and 9, at zero pathlength difference ($OPD = 0$) all the electric fields produce constructive interference regardless of their wavelength. Supposing $\bar{\lambda}$ to be the center wavelength of the spectrum of the SLD, the intensity on the detector passes from a state of constructive interference to a state of destructive interference and back to constructive interference, each time the OPD is a multiple integer of $\bar{\lambda}$. However, as soon as the OPD changes from zero, each component (harmonic) of the spectrum of the SLD suffers a phase shift that depends on its specific wavelength resulting in a partially destructive addition of the harmonics and a consequent drop in the fringe depth on the interferogram. When the OPD grows large enough, the addition of elementary harmonics is nearly totally destructive, and the interferogram remains at its constant average value.

As a result, to recover the Target position x_{Target}, the Mr is moved at constant speed v_{scan} looking for the maximum of the generated interferometric signal, which corresponds to a null OPD. Therefore, the Pa output is processed by the envelope detector ED, the derivative circuit TD, and the zero-crossing discriminator ZCD. Digital output V_O changes its logic level at the time t^* in which the interferometric signal reaches its maximum. This time instant corresponds to the condition in which the length of the reference and measuring arms are equal ($OPD = 0$). Hence, fixing the origin of the reference system where BS divides the two beams,

$$x_{Target} = x_{Mr}(t^*) = x_{Mr}(t_{start}) + v_{scan} \cdot (t^* - t_{start}) \,, \quad (8)$$

This article has been accepted for publication in a future issue of this journal, but has not been fully edited. Content may change prior to final publication. Citation information: DOI 10.1109/TIM.2019.2956421, IEEE Transactions on Instrumentation and Measurement

where, according to Fig. 3 $x_{Mr} \cdot n$ and $x_{Target} \cdot n$ are the optical path lengths BS-Mr and BS-Target, respectively. The second equality in (8) has been obtained supposing v_{scan} to be constant as in our setup. Note that the scanning speed v_{scan} of the mirror Mr must be chosen to ensure that the interferometric signal is minimally attenuated by Pa.

Indeed, according to (5) the frequency of the interferometric signal depends on the wavelength λ and the scanning speed v_{scan}. In fact, as in classic Michelson's interferometers, a Mr movement of $\bar{\lambda}/2$ corresponds to an interferometric signal period. Therefore, the interferometric signal frequency f_{Int} is:

$$f_{Int} = \frac{2v_{scan} \cdot n}{\bar{\lambda}}, \tag{9}$$

where $\bar{\lambda} \approx 834$ nm is the central wavelength of the emission spectrum in a vacuum under optical-feedback (see Fig. 5). This frequency must be much lower than the bandwidth of Pa.

In this development phase, the functional blocks for estimating the envelope and calculating the derivative have been implemented numerically. The Pa output signal was acquired by an acquisition board (National Instruments Elvis Board) with a sampling frequency f_s of 10 kHz. Then, the ED block has been realized by using the Matlab function

```
envelope(y, np, 'peak')
```  (10)

where `envelope` returns the upper and lower peak envelopes of `y` determined using spline interpolation over local maxima separated by at least `np` samples.

Similarly, TD has been numerically realized by simply calculating differences between adjacent elements and dividing them by the sampling period $(1/f_s)$.

The settings of the measuring system are resumed in Table I.

TABLE I
SETTINGS OF THE MEASURING SYSTEM (DETERMINED ACCORDING TO THE RESULTS REPORTED IN SECTION IV).

Quantity	Value
i_{SLD}	90 mA
SLD working temperature	25°C
v_{scan}	33.2 μm/s
f_s	10 kHz

C. Experimental Activities

Preliminary experimental activities have been aimed at both characterizing the electronics and the optical source composing the measuring system and defining the proper working conditions in terms of scanning speed v_{scan} and current i_{SLD} feeding the SLD.

According to subsection II-C, SLDs have relevant sensitivity to optical-feedback. Due to variations of optical gain, saturated gain and coupling efficiency between the SLD and the fiber, each SLD model may display differences in absolute values of feedback-induced changes of output power, PD monitor current (intensity of the interferometric signal) and emitting spectrum. On the other hand, SLDs have exponential dependence of power versus the feeding current, hence it's important to set the working current i_{SLD} in the linear region, well beyond the knee of the curve.

As a result, the feeding current i_{SLD} has been determined by analyzing the power versus feeding current. Then, "weak feedback condition" was verified by acquiring the SLD emission spectrum under optical-feedback exploiting the "optional block" previously shown in Fig. 3. According to subsection II-C, to high optical-feedback not only may damage the sourse, but also modify l_c and give rise to relevant subpeaks in coherence function.

According to subsection III-B, the scanning speed v_{scan} is limited by the bandwidth of Pa thus, once determined the feeding current i_{SLD} experimental activities have been aimed at experimentally determining such bandwidth.

By manually moving the mirror Mr, the condition $OPD \approx 0$ was determined. Thus, powering the loudspeaker, at the output of Pa it was possible to observe the interferometric signal whose frequency f_{Int} was a function of the amplitude and frequency of the loudspeaker driving signal Fg. The transfer function of Pa was thus estimated by keeping the Fg amplitude fixed and varying its frequency to obtain a frequency scan of the interferometric signal from 20 Hz to 10 kHz hence determining the cutoff frequency f_{Cutoff} at -3 dB.

To minimize the interferometric signal attenuation, the speed v_{scan} was then verified to satisfy the condition $f_{Int} \leq f_{Cutoff}/10$.

IV. RESULTS

Experimental activities have been performed according to the measurement procedure reported in subsection III-B and the methods reported in subsection III-C.

As discussed in subsection III-C, the first activities have been aimed at defining the feeding current i_{SLD}. Preliminary tests showed that a current i_{SLD} = 90 mA guarantees to work within the linear region beyond the knee of the curve. Fig. 5 show the power spectral densities obtained with and without optical-feedback. As expected, the OF slightly modifies the emission spectrum both in terms of shape and ripple as shown in Fig. 5. Indeed, as discussed in subsection II-C, SLD spectra generally exhibit a residual parasitic Fabry-Perot modulation that is amplified by the optical-feedback. Nevertheless, both the central wavelength $\bar{\lambda}$ and the width $\Delta\lambda$ of the emission spectrum under optical-feedback are similar to ones obtained without optical-feedback thus confirming the "weak optical-feedback condition". It is interesting to notice that, given the nominal effective refractive index $n^* \approx 3.7$ and cavity length $L_a \in (1250, 1350)$ μm declared by the manufacturer, from (4) the parasitic Fabry-Perot modulation was expected to be $\lambda_{FSR} \in (69, 75)$ pm. Considering that n^* varies as a function of quantities such as temperature and feeding current i_{SLD}, the ≈ 68 pm shown in Fig. 5 are substantially compatible with the expected λ_{FSR}.

As discussed in subsection III-C, the scanning speed v_{scan} is limited by the bandwidth of Pa, thus such bandwidth has been experimentally determined using the setup shown in Fig. 3. As an example, Fig. 6 shows the superb interferometric signal V1 observed at the output of Pa (the signal at point ① in Fig. 3)

This article has been accepted for publication in a future issue of this journal, but has not been fully edited. Content may change prior to final publication. Citation information: DOI 10.1109/TIM.2019.2956421, IEEE Transactions on Instrumentation and Measurement

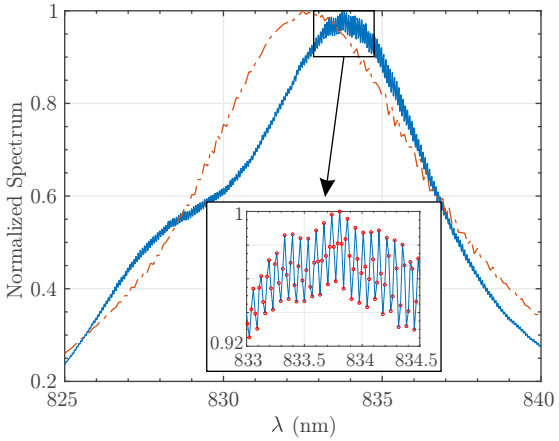

Fig. 5. Normalized emission spectra obtained with (—) and without optical-feedback (– · –) at 25°C and i_{SLD} = 90 mA. The zoom shows in more detail the ripple caused by optical-feedback (dots in the zoom represent the experimental data). As shown, the central wavelength is $\bar{\lambda} \approx 833.8$ nm and the parasitic Fabry-Perot modulation is $\lambda_{FSR} \approx 68$ pm (OSA resolution 17 pm). According to (3) the coherence length l_c in air is ≈ 45 μm.

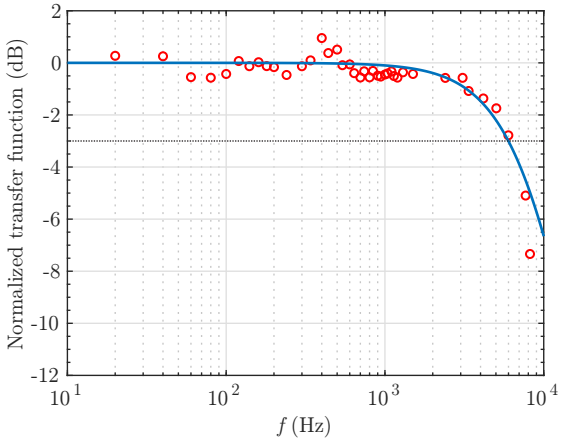

Fig. 7. Normalized frequency response of the transimpedance preamplifier Pa. The bold line represents the best Lorentzian fit to the data. The cutoff frequency f_{Cutoff} at -3dB is about 6 kHz.

when Mr was positioned to obtain the condition $OPD \approx 0$ and the loudspeaker was feed with a sinusoidal signal. As described in subsection III-C, the frequency response has been estimated by varying the frequency of the loudspeaker driving signal to obtain a frequency scan of the interferometric signal from 20 Hz to 10 kHz. The normalized frequency response so obtained is shown in Fig. 7. The figure shows the experimental data and the best Lorentzian fit. The Pa cutoff frequency f_{Cutoff} at -3dB was estimated to be 6 kHz.
Given v_{scan} = 33 μm/s, according to (9) the expected interferometric signal frequency f_{Int} is about 80 Hz, thus fully satisfying the requirement $f_{Int} \leq f_{Cutoff}/10$.

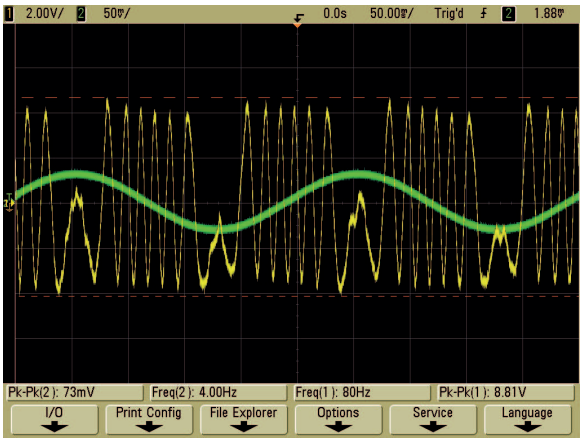

Fig. 6. Typical interferometric signal observed at the output of Pa: the "high-frequency" yellow oscilloscope trace indicates the signal at the output of Pa while the bolt green one shows the signal used to drive the loudspeaker.

In Fig. 8 is shown the signal V1 at the output of Pa acquired during a scan of Mr at constant speed v_{scan} once the loudspeaker was switched off. At time t^* a huge interferometric signal identifying the condition $OPD = 0$ is well visible.
As discussed in subsection II-C, the side-lobes in Fig. 8 are due to parasitic Fabry-Perot modulation. From Fig. 8 the cavity length can be estimated as $L_a = \Delta L/2n^* \approx 1.4$ mm which is substantially compatible with the nominal L_a declared by the manufacturer given the uncertainty on n^*.

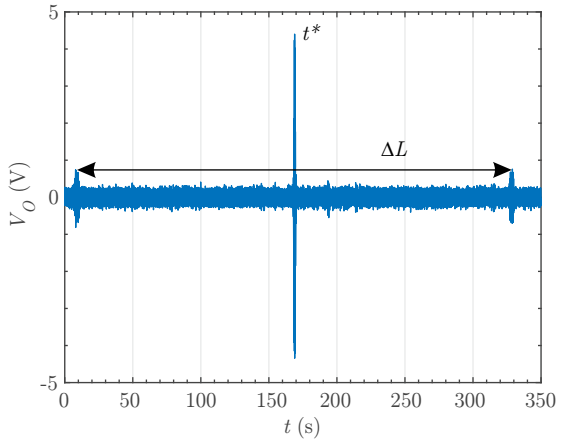

Fig. 8. Signal V1 at the output of Pa. At time t^* a huge interferometric signal identifying the condition $OPD = 0$ is well visible. Considering the scanning speed v_{scan}, the distances ΔL between points a and b is about 10.62 mm.

As discussed in subsection III-B, the envelope V2 (the signal at point ② in Fig. 3) is exploited to determine t^* and thus the Target position according to (8).
To properly follow V1, the envelope V2 shown in Fig. 9 has been realized by setting `np` (see (10)) to obtain spline interpolation over a number of samples equal to half plus 1 the number of samples composing the V1 period ($1/f_{Int}$). Note that the high-frequency noise on V2 will be largely amplified by the temporal derivative function, thus it is mandatory to perform appropriate filtering.
Fig. 10 shows the signal $V2_{filter}$ obtained by filtering with a moving average of duration equal to $25/f_{Int}$ (≈ 310 ms thus equal to about $1/2$ of the theoretical FWHM duration of the envelope — see (36)) the envelope V2 shown in Fig. 9. In the same figure, the time derivative of $V2_{filter}$ is also shown. In particular, $V3_{filter}$ has been obtained filtering V3 (the time derivative of $V2_{filter}$) with the same moving average used for

This article has been accepted for publication in a future issue of this journal, but has not been fully edited. Content may change prior to final publication. Citation information: DOI 10.1109/TIM.2019.2956421, IEEE Transactions on Instrumentation and Measurement

V2. Note that delays introduced by filtration are compensated during calibration. Neglecting such delays, from (8) the target position relative to the interferometric signal shown in Fig. 10 can be easily estimated given $t_{start} = 0$ and $x_{Mr}(t_{start}) = 30$ mm

$$x_{Target} = x_{Mr}(t_{start}) + v_{scan} \cdot (t^* - t_{start}) \approx 35.62 \text{ mm} , \quad (11)$$

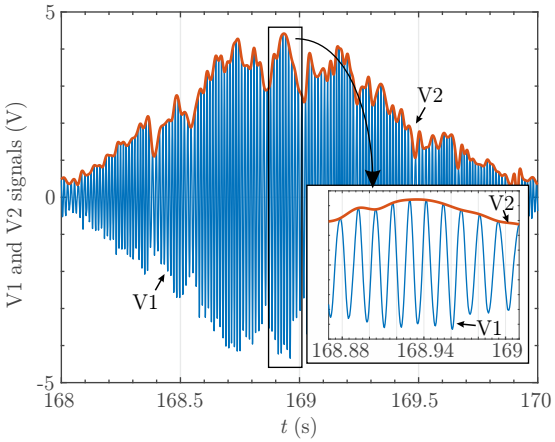

Fig. 9. Envelope V2 (—) of signal V1 (—) obtained with np equal to half plus 1 the number of samples composing the V1 period. High-frequency noise in the envelope must be properly filtered before performing the time derivative. The zoom allows to see the interferometric signal V1 in more detail. Reminding that a period of V1 corresponds to a mirror displacement equal to $\bar{\lambda}/2$, from v_{scan} it is possible to estimate $\bar{\lambda} \approx 835$ nm. Such value is substantially in agreement with Fig. 5.

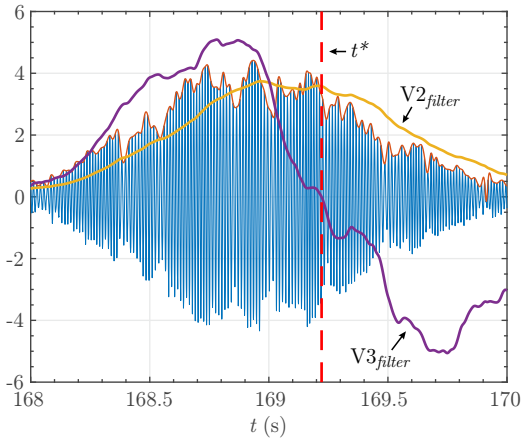

Fig. 10. Signal $V2_{filter}$ (—) obtained with a moving average of duration equal to $25/f_{Int}$ and the corresponding time derivative filtered with the same moving average $V3_{filter}$ (—). The vertical line (– – –) represents the zero crossing of $V3_{filter}$. In the figure, $V2_{filter}$ is represented in V, whereas $V3_{filter}$ is represented in V/s.

A. Crossing uncertainty

According to (8), the main contributory sources of uncertainty are related to the knowledge of the position $x_{Mr}(t)$ and the time t^*. Both are strictly related to the chosen translation stage for Mr, electronics and/or software. Assuming the use of a precision translation stage, the main cause of measurement uncertainty is the temporal determination of t^*.

The crossing uncertainty can be calculated in terms of timing jitter using the "triangular rule" [38]:

$$u_c(t^*) = \left| \frac{\sigma_{V3}|_{t=t^*}}{\frac{dV3}{dt}|_{t=t^*}} \right| , \quad (12)$$

where σ_{V3} is the noise root mean square of V3. In the case that the signal at the Pa output is sampled for subsequent numerical processing, the total temporal uncertainty must include also the uncertainty due to the sampling given by

$$u_s(t^*) = \frac{1}{\sqrt{12} f_c}, \quad (13)$$

where f_c is the sampling frequency.

In the example presented in Fig. 10, we estimated a slope of $V3_{filter}$ equal to -12.1 V/s^2 and a noise root mean square equal to 0.590 V/s, thus the crossing uncertainty is $u_c(t^*) = 48.8$ ms. In particular, as shown in Fig. 11 the slope has been estimated as the slope of the linear fitting f1 between the maximum and the minimum of $V3_{filter}$ and the noise root mean square as the root mean square of the distances between $V3_{filter}(t)$ and $f1(t)$ [38].

Having sampled the signal at 10 kHz, the sampling uncertainty is 30μs and thus it can be neglected.

Assuming the uncertainty associated with $x_{Mr}(t_{start})$, t_{start} and v_{scan} to be negligible, the combined standard measurement uncertainty relative to the Target position can be calculated from (8) as

$$u(x_{Target}) = v_{scan} \cdot u_c(t^*) = 1.6 \ \mu\text{m} , \quad (14)$$

thus the expanded uncertainty is about 3.1 μm supposing normal distribution and a coverage probability of 95%.

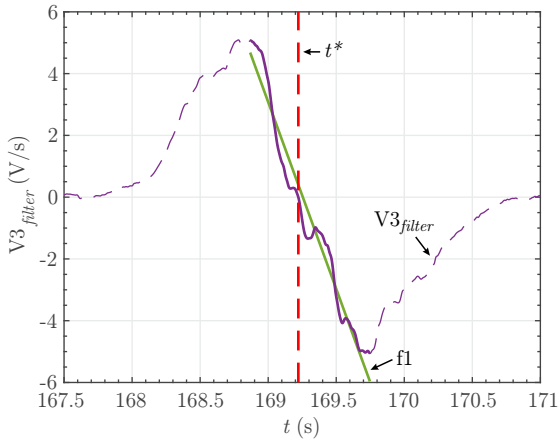

Fig. 11. $V3_{filter}$ (—) and the linear fitting f1 (—) between its maximum and minimum. The vertical line (– – –) represents the zero crossing of $V3_{filter}$.

V. Discussion and Conclusions

SM interferometry offers minimal optical part-count and excellent performances in distance and displacement measurements as discussed in subsection II-A. Also others non-contact optical techniques such as intensity-based, triangulation, time-of-flight (ToF), confocal and "classic" interferometry are available for distance and displacement measurements [39]. Such

This article has been accepted for publication in a future issue of this journal, but has not been fully edited. Content may change prior to final publication. Citation information: DOI 10.1109/TIM.2019.2956421, IEEE Transactions on Instrumentation and Measurement

techniques offer measuring intervals from a few millimeters up to kilometers with a resolution to measuring interval ratio typically in the order of magnitude of thousands — see [39]. However, intensity-based are known to suffer from the following limitations [39]: i) must be calibrated for all target objects, ii) are prone to errors related to intensity variations due to quantities such as the tilt of the target object, the variation of the target reflectivity or dust and dirt. ToF systems traditionally have a minimum working distance of at least some tens of centimeters and measurement uncertainty in the order of magnitude of millimeters. Triangulation systems do not work well with clear or transparent targets and are not able to measure through narrow openings [39]. Confocal and coherent interferometry (both SM and "classic") are prone to errors once operating in environments where the target is buried into absorbing and diffusive media how it happens in biological media or industrial applications where scatterers such as dust make measurements with coherent sources impossible.

In such circumstances, low-coherence sources are recognized to provide better performances. Indeed, low-coherence interferometers exploiting SLDs are at the basis of OCT where the reference and measurement arms interfere on high-sensitivity and low-noise detectors to extract the interferometric signal.

In this paper, we investigate and demonstrate the feasibility of an absolute distance interferometer based on the OF into a SLD cavity.

The reported results showed how the spatial localization of the interferometric signal can be extremely facilitated by the OF into the cavity. Indeed, thanks to the optical gain provided by the active region of the source it has been possible to obtain interference fringes with high visibility even with diffusive targets and without using expensive photodetectors, but directly exploiting the PD incorporated into the SLD package.

It is also important to notice that we introduced a 1.6 OD neutral density filter in the measurement arm. Considering the round-trip propagation such corresponds to an attenuation of more than 1500 times. Thus, thanks to the use of OF the system is expected not only to be able to work with diffusive and low reflectance targets, but also to operate in environments where the target is buried into absorbing and diffusive media how it happens in biological media or industrial applications where scatterers such as dust make measurements with coherent sources impossible.

As discussed in subsection II-A, once the target is buried into diffusive media low-coherence is mandatory. Actually, also OF in coherent sources allows to greatly amplify the returning signal, but given the high coherence of the source, eventual stray-light generated by scatterers along the optical path and re-entering the source cavity gives rise to tremendous noise in the interferometric signal that in turn makes measurements impossible.

On the contrary, according to (5), only fields having $OPD \leq l_c$ gives rise to the interferometric signal as it happens in OCT. Thanks to OF (SM) in low-coherence sources most of the advantages of SM-LD can be obtained and extended for absolute distance measurements in "hostile environments" where scatterers along the optical path make coherent measurements impossible. The price to pay is an increased complexity and number of components with respect to SM-LD as evident from the comparison of Figs. 1 and 2. Nevertheless, OF in low-coherence sources offers clear advantages in terms of cost and complexity with respect to "classic" OCT systems.

In this work, we focused our effort on the system feasibility demonstrating an excellent measurement uncertainty and investigating the ultimate system performances in appendix A. The described measuring system suffers substantially from all sources of uncertainty and error typical of interferometric systems except for: i) cyclic error (given the low coherence of the source) and, ii) index of refraction of the propagation medium (as long as Mr and target are immersed in the same medium at the same temperature), thus resulting less sensitive to temperature. After several much larger sources of uncertainty such as the cosine error have been appropriately cured, according to the previous discussion, measuring interval, measurement uncertainty and "response time" are mainly determined by the precision translation stage use for moving Mr.

Nowadays several motorized precision translation stages are available. As an example, LMS-270KMAX by PI (linear motor) allows up to 1000 mm travel range with speed up to 800 mm/s and nominal "Bidirectional repeatability" down to ± 150 nm. Also stages based on piezo motor such as U-523 by PI offer relevant performances (220 mm/s speed and "Bidirectional repeatability" of ± 200 nm) with a compact layout, but generally with a reduced travel (U-523 has 22 mm travel range). Thus, the uncertainty relative to the Mr position $x_{Mr}(t)$ can be made substantially negligible. Considering only crossing uncertainty, for the interferometer presented in this paper we estimated an expanded uncertainty equal to about 3.1 μm (see subsection IV-A) that gives rise to a measurement uncertainty to measuring interval ratio of about 60 ppm if considering the about 50 mm travel range of our experimental setup.

The proposed signal processing is based on the zero-crossing approach, thus it can be realized both in an analog or numerical form obtaining excellent metrological performance. The presented system has a very long "response time" (measurement time) substantially due to our Mr scanning system. Consequently, the presented system can be used only to perform measurements on quasi-static targets. This aspect can be improved enormously. Indeed, the low gain required to amplify the photocurrent signal generated by PD allows us to design the preamplifier Pa to process high-frequency interferometric signals. Consequently, as described in more detail in appendix A, the ultimate limits in terms of measuring interval and response time will be governed by the range and scanning speed of Mr.

Note also that moving parts of the interferometer could be removed exploiting a spectral domain approach as in Fourier-domain OCT.

Obviously, to perform absolute distance measurements the system needs to be carefully calibrated. Calibration and validation can be performed as an example by calibrating it against a reference measuring system such as incremental interferometers, or by using a calibrated translation stage.

This article has been accepted for publication in a future issue of this journal, but has not been fully edited. Content may change prior to final publication. Citation information: DOI 10.1109/TIM.2019.2956421, IEEE Transactions on Instrumentation and Measurement

ACKNOWLEDGMENT

The authors would like to thank E. Bonacini for his support while trying to implement the new ideas reported in this paper.

APPENDIX
ULTIMATE SYSTEM PERFORMANCES

According to (8), resolution and accuracy of the proposed measuring system depend on several quantities. A typical source of error and uncertainty for interferometric systems is the cosine error — the error arising because of the beam wave vector and the motion vector are not strictly parallel but form an angle [31]. Since in our measuring system the target distance x_{Target} is estimated as the Mr distance x_{Mr} that gives rise to $OPD = 0$ — (8) —, cosine error affects both measuring and reference arms.
After several much larger sources of uncertainty such as the cosine error have been appropriately cured, the ultimate limitation in the resolution of the proposed measuring system is determined by the quantum limit associated with the detection of the signal returning from the low-coherence interferometer. In particular, according to the procedure proposed by Donati [31], the resolution can be investigated in terms of noise-equivalent-displacement (NED) — the value of the displacement giving the same effect as the intrinsic noise.

Assuming for simplicity that a single electric field E_S is reflected by the measurand, according to (5) the AC component of the photogenerated current i_{AC} can be written as follows

$$\begin{aligned} i_{AC} =& \eta \cdot G_s \cdot 2\sqrt{P_S P_R} \cdot |\gamma(OPD)| \cdot \cos\left(\frac{2\pi OPD}{\bar{\lambda}}\right) \\ =& \eta \cdot G_s \cdot 2\sqrt{P_S P_R} \cdot |\gamma(OPD)| \cdot \cos(2\pi f_{Int} t + \varphi_0) \ , \end{aligned} \tag{15}$$

where η takes into account both the sensitivity of the photodetector and the optical coupling between the SLD and PD, P_S and P_R are the optical powers collected by the collimator CO relative to the fields E_S and E_R in (5), $|\gamma(OPD)|$ is the modulus of the complex degree of coherence — the signal we derive to estimate to estimate t^* —, t is the time from t_{start} and

$$\varphi_0 = \frac{2\pi OPD(t_{start})}{\bar{\lambda}} \ . \tag{16}$$

Thus, the voltage V1 at the input of Pa (see Fig. 3) is:

$$\mathrm{V1} = R_{TA} \cdot i_{AC} + n_1 \ , \tag{17}$$

where R_{TA} is the in-band transimpedence of the transimpedence amplifier ($R_{TA} = 50$ kΩ in our system) and n_1 takes into account noise. Equation (17) can be written as an AM signal:

$$\mathrm{V1} = A_c \cdot |\gamma(OPD)| \cdot \cos(2\pi f_{Int} t + \varphi_0) + n_1 \ , \tag{18}$$

where A_c is the amplitude of the carrier:

$$A_c = R_{TA} \cdot \eta \cdot G_s \cdot 2\sqrt{P_S P_R} \ , \tag{19}$$

and $|\gamma(OPD)|$ is the modulating signal (the "message signal"). Indeed, the coherence of the source spatially modulates the high-spatial-frequency interferometric signal with a modulation depth equal to 100%.

On the other hand, supposing the noise at the input of the envelope detector to be Gaussian, the power spectral density of the noise at the output of an envelope detector is usually approximated as [40]:

$$\begin{aligned} PSD_{ED} =& \ PSD_{n1}, \ f \in [0, 2 \cdot BW_{ED}] \\ =& \ 0, \ f > 2 \cdot BW_{ED} \ , \end{aligned} \tag{20}$$

where PSD_{n1} is the power spectral density of the noise at the input of the ED block and BW_{ED} is the bandwidth of the envelope detector.
In the following, subsection A defines the noise at the output of Pa, subsections B e C estimate the signal and noise at the output of the ED and TD blocks, respectively. The NED both for reflective and diffusive target surfaces is estimated in subsection D and the tradeoff between speed of response and noise is described in subsection E. Finally, the ultimate system performances are described in subsection F.

A. Input Noise

The input noise n_1 is mainly due to photon shot noise caused by light quantization, excess noise relative to random arrival of photons from the SLD and, thermal noise (Johnson) due to the transimpedance amplifier. Power spectral density of shot noise can be expressed as:

$$PSD_{sh} = 2|q| \cdot i_{DC} \ , \tag{21}$$

where q is the electron charge and i_{DC} is the mean detector photocurrent. Note that in SM configuration the photocurrent is generated by the photodiode PD enclosed in the same package as the optical source. Thus, under weak-feedback i_{DC} is substantially determined by the optical power emitted by the rear face of the light source P_0^* (see Fig. 2). Hence, i_{DC} substantially does not depends on P_R and P_S, thus on target and mirror positions and reflectivities, and can be approximated as a function of P_0.
On the other hand, the power spectral density of thermal noise can be expressed as:

$$PSD_{th} = \frac{4 \cdot k_B \cdot T}{R_{TA}} \ , \tag{22}$$

where k_B is the Boltzmann's constant and T is the absolute temperature. Finally, excess noise in broadband sources such as SLD can be expressed as [41]:

$$PSD_{ex} = \left(1 + \Pi^2\right) \cdot i_{DC}^2 \cdot (\Delta\nu_{eff})^{-1} \ , \tag{23}$$

where Π is the degree of source polarization and $\Delta\nu_{eff}$ is the effective optical line width of the source defined in subsection II-B.

B. Signal and Noise at ED output

The output of an ideal AM-demodulator is the modulating signal multiplied by the amplitude of the carrier, thus from (18) the voltage V_2 at the output of the ED block (see Fig. 3) is:

$$V_2 = s_{ED} + n_2 \ , \tag{24}$$

This article has been accepted for publication in a future issue of this journal, but has not been fully edited. Content may change prior to final publication. Citation information: DOI 10.1109/TIM.2019.2956421, IEEE Transactions on Instrumentation and Measurement

where the signal S_{ED} equals to

$$s_{ED} = A_c \cdot |\gamma(OPD)| \ , \tag{25}$$

and, from (20), (21), (22) and (23) the power spectral density of the noise n_2 at the output of the ED block is:

$$\begin{aligned} PSD_{ED} &= N_2, \ f \in [0, 2 \cdot BW_{ED}] \\ &= 0, \ f > 2 \cdot BW_{ED} \ , \end{aligned} \tag{26}$$

where $N_2 = PSD_{sh} + PSD_{th} + PSD_{ex}$.

C. Signal and Noise at TD output

The ideal circuit output of the TD block is the derivative of the input. Hence, from (25)

$$s_{TD} = \tau \cdot A_c \cdot \mathrm{d}\Big[|\gamma(OPD)|\Big]/\mathrm{d}t \ , \tag{27}$$

where τ is the circuit time constant. Note that (27) is valid supposing the quantities composing A_c to do not change with time. Obviously, P_R and P_S change as a function of the position of the Mr mirror and the target. Nevertheless, the interferogram develops in a length of about $2l_c$, thus for the estimate of $\mathrm{d}s_{ED}/\mathrm{d}t$ it is reasonable to assume $\mathrm{d}A_c/\mathrm{d}t = 0$. Supposing the source to have Gaussian shape, the modulus of the complex degree of coherence is [37]

$$|\gamma(OPD)| = \exp\left[-\left(\frac{\pi\Delta\lambda \cdot OPD}{\bar{\lambda}^2 \cdot 2\sqrt{\ln 2}}\right)^2\right] \ , \tag{28}$$

hence (27) becomes:

$$s_{TD} = \tau A_c \cdot \exp\left[-\left(\frac{\pi\Delta\lambda OPD}{\bar{\lambda}^2 \cdot 2\sqrt{\ln 2}}\right)^2\right] \cdot \frac{2\pi\Delta\lambda OPD}{\bar{\lambda}^2 \cdot \sqrt{\ln 2}} \cdot v_{scan} \cdot n \ . \tag{29}$$

As expected, $S_{TD} = 0$ for $OPD = 0$.

On the other hand, from (26) the variance of the noise at the output of the TD block is:

$$\begin{aligned} \sigma_{TD}^2 &= \int_0^{2BW_{ED}} (2\pi\tau f)^2 \cdot PSD_{ED} \ \mathrm{d}f \\ &= \frac{32}{3}\pi^2\tau^2 \cdot N_2 \cdot BW_{ED}^3 \ . \end{aligned} \tag{30}$$

D. NED

Supposing an ideal zero-crossing discriminator (ZCD), it is possible to define the Noise-Equivalente-Displacement (NED) as the value of the target displacement giving rise to an output variation equal to the standard deviation of the intrinsic output noise [31]. Since the proposed measurement method is based on the detection of the fringe relative to $OPD = 0$, the NED is thus equal to the OPD that satisfy the following condition:

$$\Big|s_{TD}(OPD = 0) - s_{TD}(OPD = \pm NED)\Big| = \sigma_{TD} \ , \tag{31}$$

hence

$$\frac{NED}{\sigma_{TD}} = \left(\left|\frac{\mathrm{d}s_{TD}}{\mathrm{d}OPD}\bigg|_{OPD=0}\right|\right)^{-1} = \left|\frac{\bar{\lambda}^2\sqrt{\ln 2}}{2\tau A_c \pi \Delta\lambda v_{scan} n}\right| . \tag{32}$$

The second equality in (32) has been obtained assuming $\mathrm{d}A_c/\mathrm{d}OPD \approx 0$ since the interferogram develops in a length of about $2l_c$.

It is important to notice that A_c depends on the powers P_R and P_S, thus on the positions and optical characteristics of both the target and the mirror. Since in self-mixing the same optics is used both for the emitted and collected beams, when both the mirror and the target are cooperative the collected powers are [31]:

$$\begin{aligned} P_R &= P_0 \cdot \kappa \cdot \frac{D_l^2 \cdot f_l^2}{4 \cdot d_s^2 \cdot (x_{Mr} + x_{BS})^2} \cdot r_{BS}^2 \\ P_S &= P_0 \cdot \kappa \cdot \frac{D_l^2 \cdot f_l^2}{4 \cdot d_s^2 \cdot (x_{Target} + x_{BS})^2} \cdot (1 - r_{BS})^2 \cdot T^2 \ , \end{aligned} \tag{33}$$

where κ takes into account both the transmittance of the optical fiber and the optical couplings between CO-fiber and fiber-SLD, D_l and f_l are the diameter and the focal length of the CO lens, d_s is the diameter of the fiber core (the source for CO), r_{BS} is the reflectance of the beam-splitter BS, T is the transmittance of the NDF filter (see Fig. 3) and x_{BS} is the distance of the BS from the objective lens (see Fig. 3). Equation (33) holds if both Mr and the target are large enough and do not limit the collection of radiation [31].

On the contrary, if the target is a diffusing Lambertian surface the collected power is [31]:

$$P_S = P_0 \cdot \kappa \cdot \delta \cdot \frac{D_l^2}{4(x_{Target} + x_{BS})^2} \cdot r_{BS}^2 \cdot T^2 \ , \tag{34}$$

where δ is the diffusivity of the target (the fraction of the power rediffused back by the target over the power arriving on it). Also in this case, (34) holds if the target is wider than the spot of the SLD and the NDF is large enough to do not limit the collection of the radiation.

It is also important to notice that according to (30) the variance of the noise at the output of the TD block is depends on the bandwidth of the ED. Hence, from (32) NED depends on BW_{ED}. Such aspect is investigated in subsection E.

E. Speed of response and noise tradeoff

If we define the speed of response as the time the system takes to provide an estimate of the target position, such parameter is substantially defined by both the current target position and the scanning speed v_{scan}. It is important to notice that the scanning speed defines also the frequency of the interferometric signal f_{Int} (the carrier) and the "duration" of the modulating signal $|\gamma(OPD)|$, thus the bandwidths of the Pa and ED blocks.

Supposing the source to have Gaussian shape, the modulus of the complex degree of coherence is Gaussian to as described in (28). It is known that the Fourier transform of a Gaussian function is another Gaussian function and that the FWHM of the signal in the time domain (δ_t) is related to the FWHM in the frequency domain (δ_f) by:

$$\delta_t \cdot \delta_f = \frac{2\ln 2}{\pi} \ . \tag{35}$$

This article has been accepted for publication in a future issue of this journal, but has not been fully edited. Content may change prior to final publication. Citation information: DOI 10.1109/TIM.2019.2956421, IEEE Transactions on Instrumentation and Measurement

From (28), we have:

$$\delta_t = \frac{\sqrt{2}\cdot\bar{\lambda}^2\cdot\ln 2}{\pi\cdot\Delta\lambda\cdot v_{scan}\cdot n} \;\Rightarrow\; \delta_f = \frac{\sqrt{2}\cdot\Delta\lambda\cdot v_{scan}\cdot n}{\bar{\lambda}^2} \,. \quad (36)$$

Since $BW_{ED} \geq \delta_f$, v_{scan} influences the noise at the output of the ED block, hence the NED.
By setting $BW_{ED} = \delta_f$, from (28), (30) and (35) the standard deviation of the output noise becomes:

$$\sigma_{TD} = \frac{2^{13/4}}{\sqrt{3}}\pi\tau\cdot\frac{\sqrt{N_2\Delta\lambda^3 v_{scan}^3 n^3}}{\bar{\lambda}^3} \,. \quad (37)$$

Supposing $\Delta\lambda$ = 10 nm, $\bar{\lambda}$ = 834 nm, n = 1 and v_{scan} = $33.2\cdot10^{-6}$ m/s^2, we have $BW_{ED} \approx 0.7$ Hz.

Note that for proper AM demodulation the carrier frequency must be much greater than the highest frequency component of the message signal. Such is not a limit for v_{scan} since the ratio of the spatial frequencies relative to the carrier (interferometric signal) and the message signal ($|\gamma|$) is given by the ratio $\Delta\lambda/\bar{\lambda}$.

F. Ultimate system performances

According to the discussions in previous subsections, from (32) (37) we have:

$$NED = \frac{2^{9/4}}{\sqrt{3}\cdot A_c\cdot\bar{\lambda}}\cdot\sqrt{\ln 2\cdot N_2\cdot\Delta\lambda\cdot v_{scan}\cdot n} \,. \quad (38)$$

Figures 12 and 13 show the NED estimated for our system both for cooperative and diffusing Lambertian targets. In particular, Fig. 12 shows the NED as a function of the target position x_{Target} and the output power of the source P_0, whereas Fig. 13 shows the NED as a function of the target position x_{Target} and the scanning speed v_{scan}.
Note that Figures 12 and 13 have been obtained supposing a target diffusivity δ equal to 1. Such is not a limitation since for lower target diffusivity it is possible to reduce the attenuation of the NDF (see Fig. 3). Indeed, Figures 12 and 13 has been obtained supposing $T^2 = 6.25\cdot10^{-4}$ in (34).

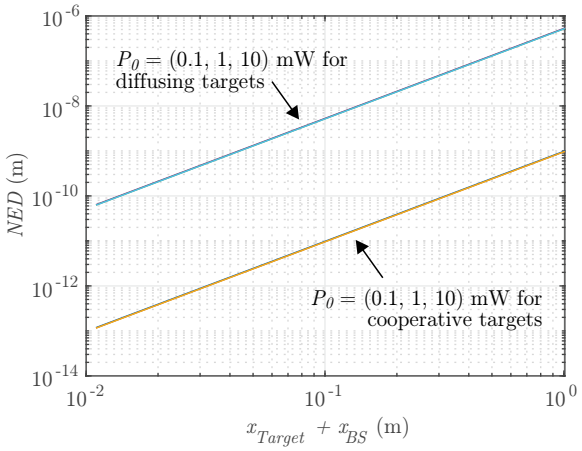

Fig. 12. NED as a function of the target position x_{Target} and the output power of the source P_0 both for cooperative and diffusing Lambertian targets. Figure shows the results obtained for v_{scan} = 33 μm/s D_l = 3 mm, f_l = 2.7 mm, d_s = 5 μm, G_s = 100, i_{DC} = 0.36 (A/W) $\cdot$ P_0, δ = 1.

It is interesting to note that, as shown in Fig. 12, in our implementation the NED is substantially independent of P_0.

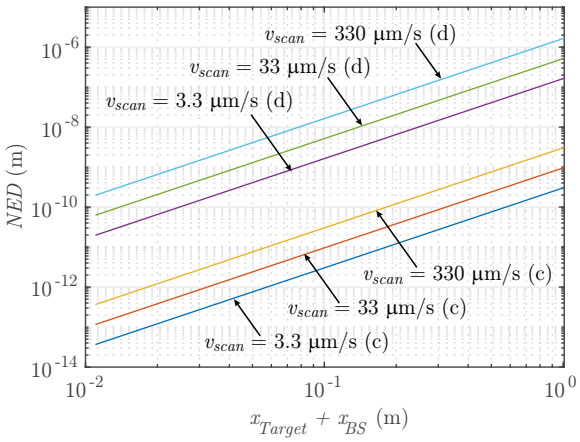

Fig. 13. NED as a function of the target position x_{Target} and the scanning speed v_{scan} both for cooperative (c) and diffusing Lambertian (d) targets. Figure shows the results obtained for P_0 = 1 mW D_l = 3 mm, f_l = 2.7 mm, d_s = 5 μm, G_s = 100, i_{DC} = 0.36 (A/W) $\cdot$ P_0, δ = 1.

Indeed, in our implementation N_2 is mainly due to PSD_{ex} which is proportional to P_0^2. Since A_c is proportional to P_0, from (38) it is easy to observe that if N_2 is dominated by PSD_{ex} the NED is substantially independent of P_0.

Note that the proposed analysis supposed that a single electric field E_S is reflected by the measurand (see (15)). An analysis of the ultimate performances of self-mixing systems in the speckle pattern regime has been proposed by Donati *et al.* [42].

REFERENCES

[1] M. Dufour, G. Lamouche, V. Detalle, B. Gauthier, and P. Sammut, "Low-coherence interferometry — an advanced technique for optical metrology in industry," *Insight: Non-Destructive Testing and Condition Monitoring*, vol. 47, no. 4, pp. 216–219, 2005.

[2] A. Obaton, Y. Sanogo, J. Lautru, M. Lievre, J. Durocher, and J. Dubard, "Development of a new optical reference technique in the field of biology," *IEEE Transactions on Instrumentation and Measurement*, vol. 62, no. 4, pp. 837–844, April 2013.

[3] C. K. Hitzenberger, "Optical coherence tomography in optics express (Invited)," *Opt. Express*, vol. 26, no. 18, pp. 24 240–24 259, Sep 2018.

[4] L. Rovati, U. Minoni, M. Bonardi, and F. Docchio, "Absolute distance measurement using comb-spectrum interferometry," *Journal of Optics*, vol. 29, no. 3, pp. 121–127, jun 1998.

[5] L. Rovati, S. Cattini, and N. Palanisamy, "Measurement of the fluid-velocity profile using a self-mixing superluminescent diode," *Measurement Science and Technology*, vol. 22, no. 2, p. 025402, 2011.

[6] Y. Mao, C. Flueraru, S. Chang, D. P. Popescu, and M. G. Sowa, "High-quality tissue imaging using a catheter-based swept-source optical coherence tomography systems with an integrated semiconductor optical amplifier," *IEEE Transactions on Instrumentation and Measurement*, vol. 60, no. 10, pp. 3376–3383, Oct 2011.

[7] K. Neuhaus, P. M. McNamara, S. Alexandrov, S. O'Gorman, J. Hogan, C. Wilson, and M. J. Leahy, "Performance review of multiple reference versus time domain optical coherence tomography," *IEEE Photonics Journal*, vol. 10, no. 3, pp. 1–14, June 2018.

[8] S. Donati and M. Norgia, "Self-mixing vibrometer has picometer sensitivity by exploiting the fm channel," in *2018 Conference on Lasers and Electro-Optics (CLEO)*, May 2018, pp. 1–2.

[9] M. Norgia, A. Pesatori, and L. Rovati, "Self-mixing laser doppler spectra of extracorporeal blood flow: A theoretical and experimental study," *Sensors Journal, IEEE*, vol. 12, no. 3, pp. 552 –557, march 2012.

[10] M. Norgia, A. Pesatori, and F. Cavedo, "Proximity sensor using self-mixing effect," in *2018 IEEE International Instrumentation and Measurement Technology Conference (I2MTC)*, May 2018, pp. 1–5.

[11] M. Norgia, A. Pesatori, and L. Rovati, "Low-cost optical flowmeter with analog front-end electronics for blood extracorporeal circulators," *Instrumentation and Measurement, IEEE Transactions on*, vol. 59, no. 5, pp. 1233–1239, 2010.

[12] M. Usman, U. Zabit, O. D. Bernal, G. Raja, and T. Bosch, "Detection of multimodal fringes for self-mixing-based vibration measurement," *IEEE Transactions on Instrumentation and Measurement*, pp. 1–10, 2019.

[13] Z. A. Khan, U. Zabit, O. D. Bernal, M. O. Ullah, and T. Bosch, "Adaptive cancellation of parasitic vibrations affecting a self-mixing interferometric laser sensor," *IEEE Transactions on Instrumentation and Measurement*, vol. 66, no. 2, pp. 332–339, Feb 2017.

[14] A. G. Demir, P. Colombo, M. Norgia, and B. Previtali, "Evaluation of self-mixing interferometry performance in the measurement of ablation depth," *IEEE Transactions on Instrumentation and Measurement*, vol. 65, no. 11, pp. 2621–2630, Nov 2016.

[15] M. Norgia, A. Pesatori, and S. Donati, "Compact laser-diode instrument for flow measurement," *IEEE Transactions on Instrumentation and Measurement*, vol. 65, no. 6, pp. 1478–1483, June 2016.

[16] A. Magnani, A. Pesatori, and M. Norgia, "Real-time self-mixing interferometer for long distances," *IEEE Transactions on Instrumentation and Measurement*, vol. 63, no. 7, pp. 1804–1809, July 2014.

[17] I. Milesi, M. Norgia, P. P. Pompilio, C. Svelto, and R. L. Dellaca, "Measurement of local chest wall displacement by a custom self-mixing laser interferometer," *IEEE Transactions on Instrumentation and Measurement*, vol. 60, no. 8, pp. 2894–2901, Aug 2011.

[18] L. Rovati, L. d. Cecilia, and S. Cattini, "Optical feedback into a superluminescent diode cavity for absolute distance measurements," in *2019 IEEE International Instrumentation and Measurement Technology Conference (I2MTC)*, May 2019, pp. 1–5.

[19] S. Donati, "Responsivity and noise of self-mixing photodetection schemes," *IEEE Journal of Quantum Electronics*, vol. 47, no. 11, pp. 1428–1433, Nov 2011.

[20] V. R. Shidlovski, "Superluminescent diodes. SLD sensitivity to optical feedback." SuperlumDiodes Ltd., Tech. Rep., 2004.

[21] F. Gouaux, N. Servagent, and T. Bosch, "Absolute distance measurement with an optical feedback interferometer," *Appl. Opt.*, vol. 37, no. 28, pp. 6684–6689, Oct 1998.

[22] M. Norgia and S. Donati, "A displacement-measuring instrument utilizing self-mixing interferometry," *IEEE Transactions on Instrumentation and Measurement*, vol. 52, no. 6, pp. 1765–1770, Dec 2003.

[23] S. Shinohara, H. Yoshida, H. Ikeda, K. Nishide, and M. Sumi, "Compact and high-precision range finder with wide dynamic range and its application," *IEEE Transactions on Instrumentation and Measurement*, vol. 41, no. 1, pp. 40–44, Feb 1992.

[24] T. Shibata, S. Shinohara, H. Ikeda, H. Yoshida, and M. Sumi, "Automatic measurement of velocity and length of moving plate using self-mixing laser diode," *IEEE Transactions on Instrumentation and Measurement*, vol. 48, no. 6, pp. 1062–1067, Dec 1999.

[25] F. Vogel and B. Toulouse, "A low-cost medium-resolution rangefinder based on the self-mixing effect in a vcsel," *IEEE Transactions on Instrumentation and Measurement*, vol. 54, no. 1, pp. 428–431, Feb 2005.

[26] C. Bes, G. Plantier, and T. Bosch, "Displacement measurements using a self-mixing laser diode under moderate feedback," *IEEE Transactions on Instrumentation and Measurement*, vol. 55, no. 4, pp. 1101–1105, Aug 2006.

[27] U. Zabit, O. D. Bernal, and T. Bosch, "Self-mixing laser sensor for large displacements: Signal recovery in the presence of speckle," *IEEE Sensors Journal*, vol. 13, no. 2, pp. 824–831, Feb 2013.

[28] M. Veng, J. Perchoux, and F. Bony, "Fringe disappearance in self-mixing interferometry laser sensors: Model and application to the absolute distance measurement scheme," *IEEE Sensors Journal*, vol. 19, no. 14, pp. 5521–5528, July 2019.

[29] S. Donati and M. Norgia, "Self-mixing interferometry for biomedical signals sensing," *IEEE Journal of Selected Topics in Quantum Electronics*, vol. 20, no. 2, pp. 104–111, March 2014.

[30] S. Donati, "Developing self-mixing interferometry for instrumentation and measurements," *Laser & Photonics Reviews*, vol. 6, no. 3, pp. 393–417, 2012.

[31] S. Donati, *Electro-Optical Instrumentation: Sensing and Measuring with Lasers*. Prentice Hall, 2004.

[32] L. Rovati and F. Docchio, "Low-coherence interferometry using a self-mixing super-luminescent diode," *Photonics Technology Letters, IEEE*, vol. 10, no. 1, pp. 123–125, 1998.

[33] L. Di Cecilia, S. Cattini, F. Giovanardi, and L. Rovati, "Single-arm self-mixing superluminescent diode interferometer for flow measurements," *Journal of Lightwave Technology*, vol. 35, no. 16, pp. 3577–3583, Aug 2017.

[34] L. Rovati, L. Pollonini, and F. Docchio, "A system for the inspection and quality control of glass slabs," *Review of Scientific Instruments*, vol. 73, no. 9, pp. 3386–3391, 2002.

[35] V. Shidlovski, "Superluminescent diodes. Short overview of device operation principles and performance parameters," SuperlumDiodes Ltd., Tech. Rep., 2004.

[36] M. Born and E. Wolf, *Principles of optics*, 7th ed. Cambridge University Press, 1999.

[37] J. Goodman, *Statistical Optics*. John Wiley and Sons, 2000.

[38] L. Rovati, M. Bonaiuti, and P. Pavan, "Design of a high-performance optical system for angular position measurement: optical and electronic strategies for uncertainty reduction," *IEEE Transactions on Instrumentation and Measurement*, vol. 54, no. 5, pp. 2075–2081, Oct 2005.

[39] G. Berkovic and E. Shafir, "Optical methods for distance and displacement measurements," *Adv. Opt. Photon.*, vol. 4, no. 4, pp. 441–471, Dec 2012.

[40] S. Haykin and M. Moher, *An Introduction to Analog and Digital Communications*. Wiley, 2006.

[41] A. F. Fercher, W. Drexler, C. K. Hitzenberger, and T. Lasser, "Optical coherence tomography — principles and applications," *Reports on Progress in Physics*, vol. 66, no. 2, p. 239, 2003.

[42] S. Donati, G. Martini, and T. Tambosso, "Speckle pattern errors in self-mixing interferometry," *IEEE Journal of Quantum Electronics*, vol. 49, no. 9, pp. 798–806, Sep. 2013.